

# Effect of Grain Size on the Tensile Deformation Mechanisms of Commercial Pure Titanium as Revealed by Acoustic Emission

*Lifei Li, Zheng Zhang, and Gongtian Shen*

*(Submitted October 14, 2014; in revised form February 11, 2015; published online March 4, 2015)*

The effect of grain size on the deformation mechanisms during different tensile stages in commercial pure titanium was investigated by acoustic emission (AE) at room temperature. The deformation mechanisms, dislocation slip, and mechanical twinning were found to be the two AE sources for all grain sizes throughout the experiments. Based on the AE features of frequency and energy, the AE signals stemming from the two deformation mechanisms were classified. As grain size increased, the AE activity and intensity attributed to twinning increased. The twinning activity was confirmed by optical microscope and scanning electron microscopy. The results showed that for the specimen with small-sized grains, the entire tensile deformation was mainly achieved by slip, and only slightly assisted by twinning. Deformation of the specimen with medium-sized grains was accomplished by combined slip and twinning. For the specimen with large grains, twinning was the more active mechanism during the early stages of the tensile tests, while slip played a larger role in the later stages of the tensile tests. This larger role of slip in the later stages occurred despite the notable increase in the amount of twinning.

**Keywords** acoustic emission, deformation mechanism, grain size, titanium

## 1. Introduction

### 1.1 Background and Purpose

As the most widely used titanium alloy in all product forms for petrochemical industrial applications, commercial pure titanium (CP-Ti) has excellent engineering properties, such as remarkable corrosion resistance, high weldability, and a good balance of moderate strength with reasonable ductility (Ref 1, 2). Despite the rapid growth in its utilization, the structural performance of CP-Ti is still not clearly understood, because of its complex deformation mechanism, which is due to its hexagonal-close-packed (hcp) lattice structure. Over the past few decades, there has been extensive research of the effects on the plastic deformation of CP-Ti by some deformation conditions and material parameters including temperature (Ref 2-4), strain rates (Ref 3, 5), mode of load (compression, tensile or simple shear deformation) (Ref 4, 6), texture or orientation (Ref 1, 7, 8), and purity (Ref 9, 10). However, the impact of grain size as a material variable on deformation in titanium has only been studied by a few researchers. It was observed that the grain size dependence of flow stress followed the Hall-Petch relationship at 575 K, but

deviated from this relationship at 295 K when under high strain (Ref 11). Based on a constitutive model for predicting the critical stress of twinning, it was found that larger grains exhibited a greater propensity for mechanical twinning than smaller grains (Ref 12). By testing titanium under tension and magnesium under compression, it was confirmed experimentally that the twinning volume fraction in titanium strongly depended on the grain size, while it was almost independent in magnesium (Ref 13). Hence, for titanium alloy, slip and twinning occur concomitantly during plastic deformation. However, the relationship between the two deformation mechanisms and with strain remains an open question.

Acoustic emission (AE) stems from the transient elastic waves, which generate within the material due to sudden irreversible structural changes (Ref 14). During the early 1980s, a number of works were devoted to the investigation of the rules governing the AE changes in the deformation of titanium (Ref 15-18). Compared with the tensile tests of  $\alpha$ -Ti and Ti-6Al-4V, Tanaka and Horiuchi (Ref 15) recognized that the AE sources included twin formation. By investigating two pure grades of  $\alpha$ -Ti, Friesel and Carpenter (Ref 16) postulated that the AE at yield or at hardening regions was due to the initiation of slip, and that the AE at strains following yield could be attributed to deformation twinning. By means of AE location and digital image correlation, Murasawa et al. (Ref 18) measured the nucleation of an intermittent twinning region around the early stage of the yield in pure Ti under uniaxial tension. Therefore, it has been confirmed that the AE technique is capable of monitoring deformation processes in real time. Since the effect of grain size on CP-Ti has not been clearly described, the present work aims to (i) identify the effect of grain size on the tensile behavior of CP-Ti, and (ii) apply AE measurements to provide a deeper insight into the activity of slip and twinning for this case of a hcp metal.

**Lifei Li** and **Zheng Zhang**, 8th Lab of the School of Material Science and Engineering, Beihang University, No. 37 Xueyuan Road, Haidian District, Beijing 100191, China; and **Gongtian Shen**, China Special Equipment Inspection and Research Institute, Beijing 100013, China. Contact e-mails: zhangzh@buaa.edu.cn, tihutihu@163.com.

## 1.2 AE Mechanism During Plastic Deformation

The AE features derived from the AE sources of slip and twinning are briefly surveyed in this section in terms of two AE parameters, energy, and frequency.

**1.2.1 AE Energy.** Chung (Ref 19) calculated the AE radiation energy ( $E_t$ ) due to the dislocation per unit length

$$E_t \cong K_{is} v^2 \ln(\tau/\tau_0) = \frac{\mu b^2}{4\pi c_t^2} v^2 \ln(\tau/\tau_0) \quad (\text{Eq 1})$$

$$E_t \cong K_{ie} v^2 \ln(\tau/\tau_0) = \frac{\mu b^2}{2\pi} \left( \frac{1}{c_t^2} - \frac{1}{2c_s^2} \right) v^2 \ln(\tau/\tau_0), \quad (\text{Eq 2})$$

where  $\mu$  is the shear modulus,  $b$  is Burgers vector,  $c_l$  and  $c_t$  are the longitudinal and shear wave velocities, respectively,  $v$  is the velocity of the dislocation, and  $\tau$  is the time for dislocation motion, such that  $c_t \tau_0 = b$ . Equations 1 and 2 represent a screw dislocation and an edge dislocation, respectively. Considering a polycrystalline material under a constant strain rate, whose plastic deformation is completed only by dislocation motion, it presumed that

$$\rho_m v = \text{constant}, \quad (\text{Eq 3})$$

where  $\rho_m$  is the total mobile dislocation density. Changing the grain size will change the dislocation motion and thus alter the AE generation. Since the dislocation glide distance is confined by a grain diameter,  $\rho_m$  can be expressed as

$$\rho_m = \rho_{mg} + \rho_0 = A/D + \rho_0. \quad (\text{Eq 4})$$

In Eq 4,  $\rho_0$  is the intragranular mobile dislocation density,  $\rho_{mg}$  is the mobile dislocation density from grain boundary,  $D$  is the average grain size, and  $A$  is a constant. The energy of the AE source  $E_{AE}$ , attributed to the dislocation motion, is described as Eq 5 in terms of the number of moving dislocations and the radiation wave energy  $E_t$  as given by Eq 1 and 2 (Ref 19). The duration time of such dislocation motion  $\tau$  is given by Eq 6.

$$E_{AE} = \rho_m E_t \quad (\text{Eq 5})$$

$$T = D/v. \quad (\text{Eq 6})$$

Thus, substituting Eq 1 or 2 and Eq 3, 4, and 6 into Eq 5, the relationship between  $E_{AE}$  and  $D$  can be described as

$$E_{AE} \propto \frac{1}{\frac{A}{D} + \rho_0} \quad (\text{Eq 7})$$

According to Eq 7, the energy of the AE source increases with increasing grain size. Kiesewetter et al. (Ref 20) and Scruby et al. (Ref 21) experimentally observed that the AE signal energy from the deformation of pure aluminum increased with the grain size growth.

A lenticular twinning can be modeled as a pile-up of  $N$  dislocations of length  $L$  distributed within a distance  $S$  equivalent to the thickness of the twinning (Ref 22). The condition  $S \gg L$  implies that twinning is created by the coherent motion of a large number of dislocation segments. This suggests that twinning is associated with a higher energy of corresponding AE signal than dislocation.

**1.2.2 AE Frequency.** Fleischmann et al. (Ref 23) estimated the frequency spectrum of the ultrasonic waves produced by a moving dislocation. It was assumed that dislocation moved at a constant velocity  $v$  from the onset of motion until an

**Table 1** Annealing treatment and resulting grain size

Average grain size, $D$ , $\mu\text{m}$	Annealing temperature, K	Annealing time, min	Cooling condition
26	As received		
45	923	120	Air cooling
93	1073	600	Furnace cooling

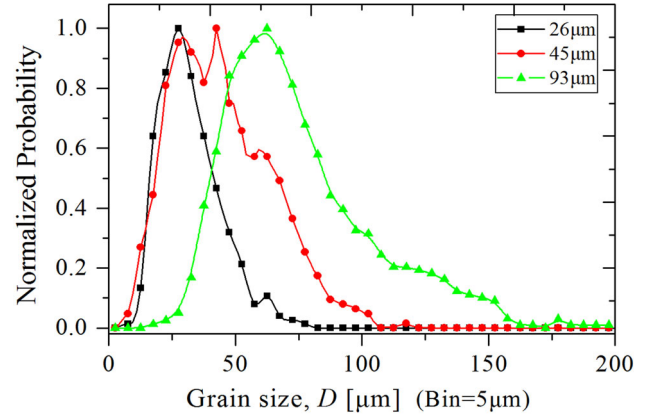


**Fig. 1** Normalized probability for grain size under three conditions

obstacle terminated the motion after traveling a distance  $d$ . The AE from such source was within a certain frequency bandwidth, which had a upper frequency limit  $f_{up}$  described as

$$f_{up} = v/2d \quad (\text{Eq 8})$$

Grain size growth causes the glide distance  $d$  to increase and the dislocation velocity  $v$  to decrease (Ref 24). The resulting larger grains then cause a shift in the frequency distribution of the elastic waves, which are released by a moving dislocation, to a lower frequency band.

Moorthy et al. (Ref 25) modeled a new dislocation loop with a Frank-Read source and described the AE event lifetime  $t$  as:

$$t = \left( \frac{3}{4} N \cdot \frac{7}{8} \cdot \frac{D}{2} \right) / v, \quad (\text{Eq 9})$$

where  $N$  is the total number of dislocations in the pile-up. According to the relationship  $t \propto 1/(2f)$ , Eq 9 shows that increasing  $D$  can induce an increase of  $t$  and a shift of the AE signal frequency  $f$  to lower values. Therefore, either the moving dislocation or the growth of a dislocation loop within a bigger grain size will result in a shift of the AE frequency to a lower range.

The initial of twinning nucleation and growth proceeds on the order of sonic velocity, which is higher than the speed of dislocation motion. Subsequently, as modeled by a pile-up of dislocations described previously, lenticular twinning has a larger number  $N$  and a higher velocity  $v$  and occurs within a shorter timespan than does dislocation motion. Therefore, twinning results in higher frequency band compared with that of slip. For zirconium (Ref 26) and magnesium alloy (Ref 27, 28) under tensile or compressive strain, it has been found experimentally that the AE signals due to twinning exhibit a higher frequency than does slip.

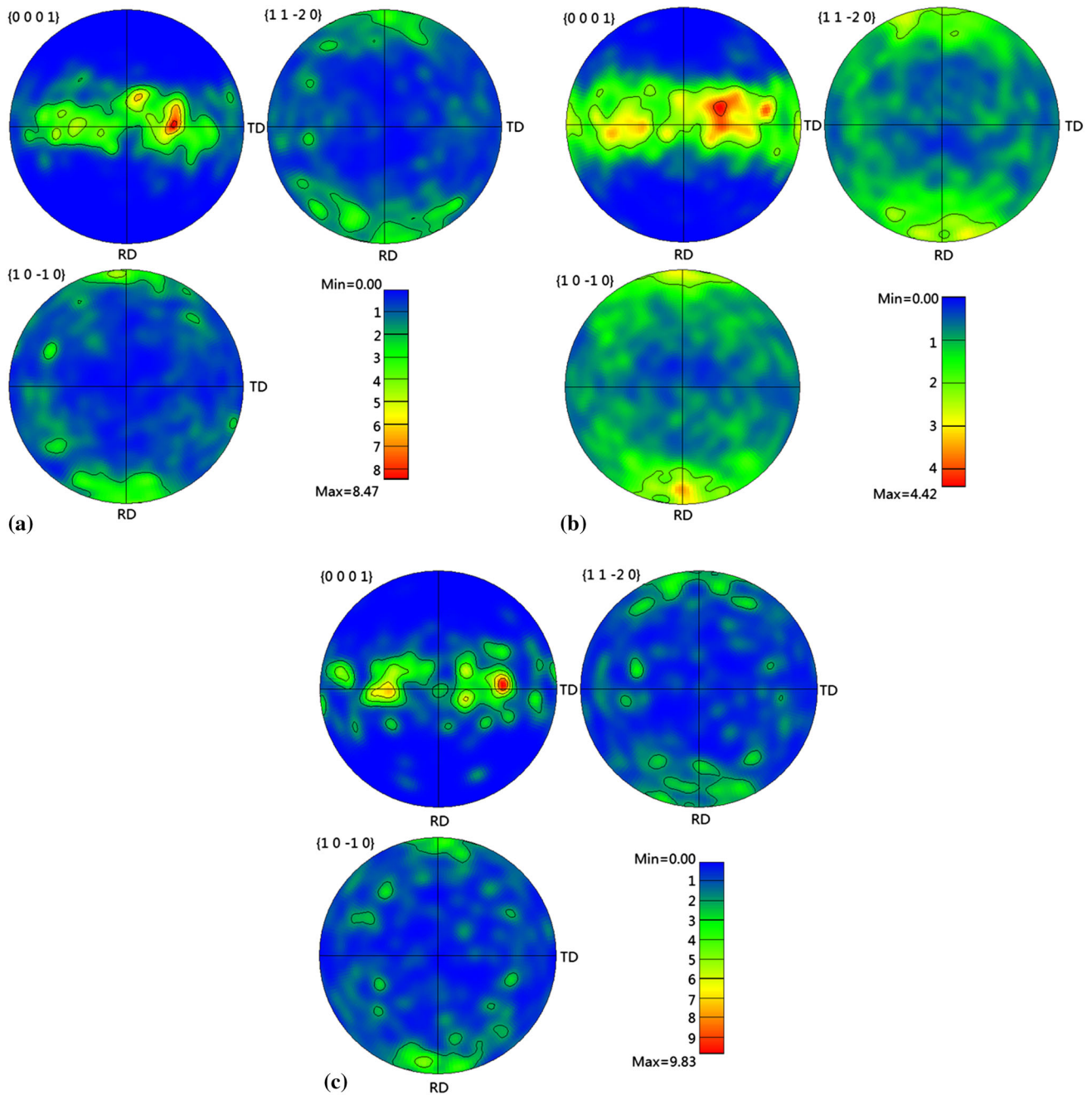


**Fig. 2** EBSD pole figures of starting specimens for (a)  $D = 26$ , (b)  $D = 45$ , and (c)  $D = 93 \mu\text{m}$

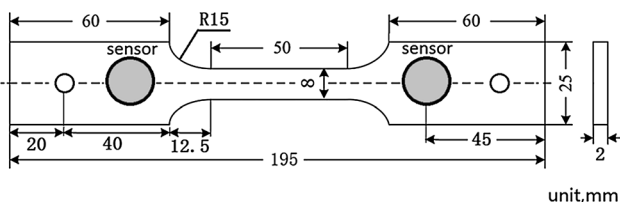


**Fig. 3** Dimensions of tensile specimen showing sensor position

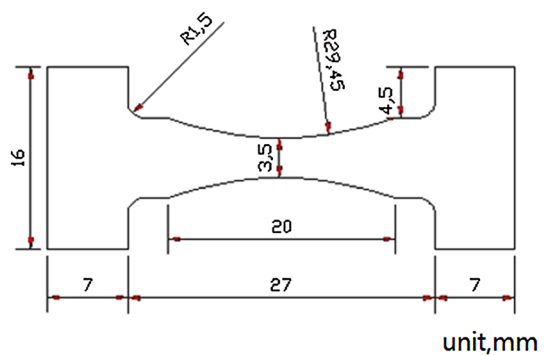


**Fig. 4** Configuration of small specimen for in situ SEM tensile test

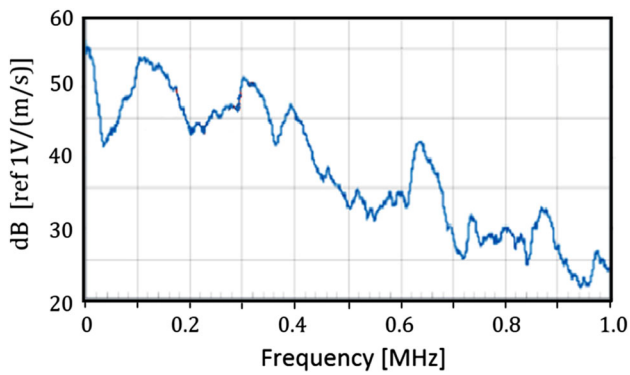


Fig. 5 Frequency response curve of WD sensor

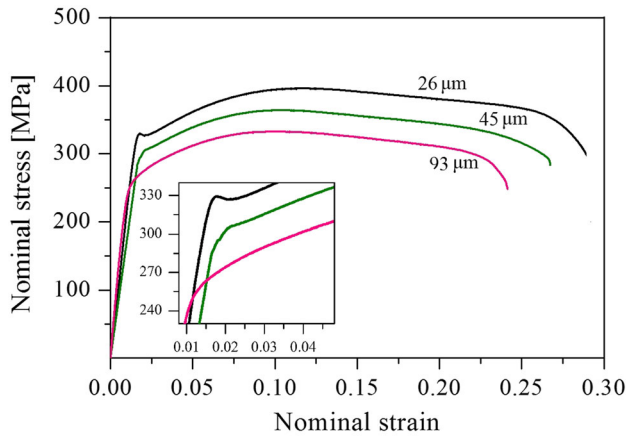


Fig. 6 Stress-strain curves for different average grain sizes

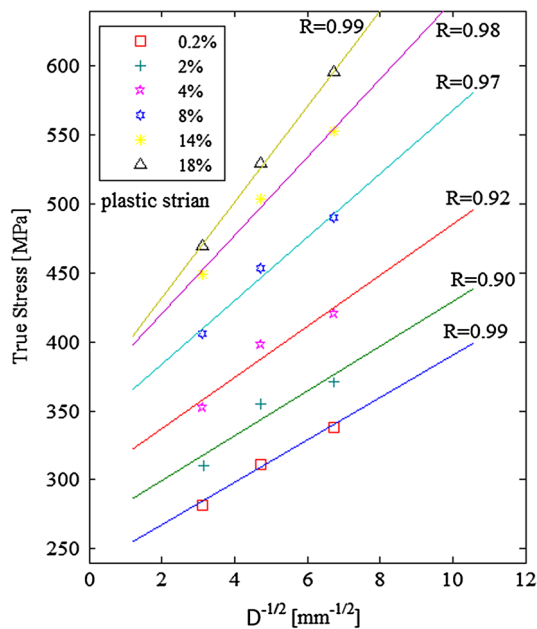


Fig. 7 Variation of the true stress with the inverse square root of grain size

## 2. Experimental Materials and Methods

### 2.1 Materials

As-received annealed CP-Ti Grade 2, code TA2 (0.028Fe, 0.009C, 0.002H, 0.009N, and 0.11O, all in wt.%), was supplied in the form of an 8-mm-thick plate. The required grain size variation was obtained by various recrystallization-annealing treatments under vacuum (Table 1). Figure 1 illustrates the normalized probability of grain size based on the statistics from 2500 to 3000 crystal grains. The grain sizes for the specimens with  $D = 26 \mu\text{m}$  and  $D = 93 \mu\text{m}$  are relatively homogenous. On the other hand, for the specimen with  $D = 45 \mu\text{m}$ , the probability shows two main sizes. This is because the  $D = 45 \mu\text{m}$  specimen was acquired during the process of grain growth, while the  $D = 93 \mu\text{m}$  specimen was in the late stage of grain growth. The initial microstructure of the specimens all exhibited a single  $\alpha$ -phase with nearly equiaxed grains without twinning. For titanium alloys, the activation of the twin depends on the initial texture (Ref 1, 7, 8). Figure 2 shows the pole figures of the specimens for more than 1000 grains before tension. The  $\{0\ 0\ 0\ 1\}$  pole figures of the three all have a texture with the maxima inclined  $25^\circ$ – $40^\circ$  from ND towards  $\pm$  TD, distributed with the spread of the rolled texture. The  $\{1\ 1\ -2\ 0\}$  and  $\{1\ 0\ -1\ 0\}$  pole figures show again that the overall textures of the specimens with  $D = 45 \mu\text{m}$  and  $D = 93 \mu\text{m}$  are still quite similar to the one with  $D = 26 \mu\text{m}$ .

### 2.2 Tensile Tests

The tensile specimens were machined from the plate parallel to the rolling direction, and the dimensions are shown in Fig. 3. The tensile tests were carried out at room temperature (300 K) using a SANSI test machine at a strain rate of  $1.67 \times 10^{-4} \text{ s}^{-1}$ . The repeated experiments showed a consistent result, with the variation between stress-strain curves being better than  $\pm 6$  pct. To investigate the microstructure development, some tensile tests were interrupted at different deformation stages, and the twinning volume fractions were calculated based on optical micrographs. Furthermore, to acquire the microstructure evo-

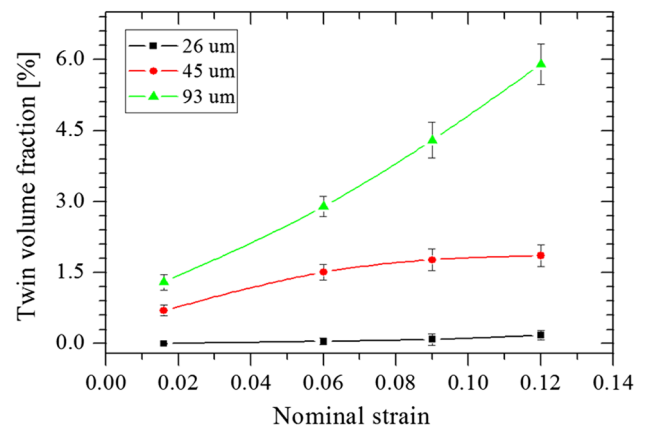
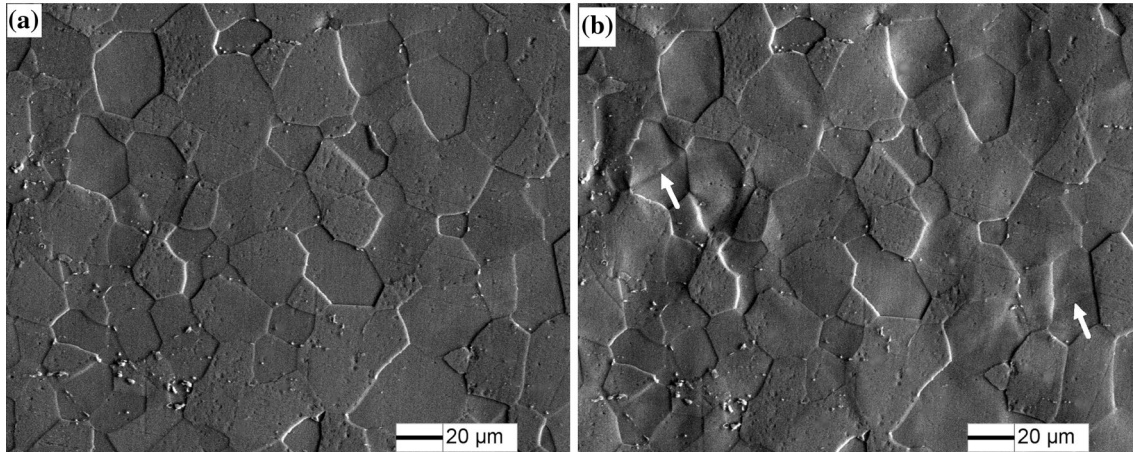
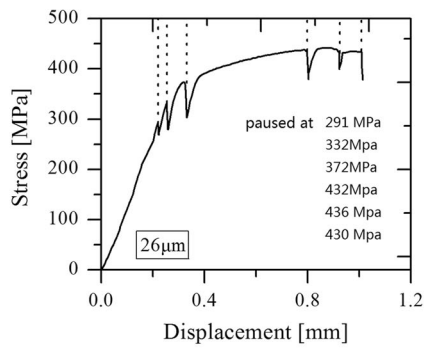


Fig. 8 Twinning volume fractions ( $T_V$ ) for different grain sizes and strains



**Fig. 9** Sequential SEM micrographs for the  $D = 26 \mu\text{m}$  specimen at (a) 436, and (b) 430 MPa

lution in real time, especially during the stage of yield, in situ observations of small flat dog-bone-shaped samples (Fig. 4) under tension by scanning electron microscopy (SEM) were employed. A reduction was introduced in the gage section to ensure the plastic deformation mainly occurred at the center area, and the in situ deformation could be captured. The experiments were performed in a chamber of a SEM equipment (Mode: CS3400, CamScan Ltd., Britain), using displacement control at a rate of 0.02 mm/min. Microstructure observations were made on the etched specimens in the backscattered electron (BSE) imaging mode.

### 2.3 AE Equipment

AE signals generated during the tensile deformation were recorded and analyzed using a DiSP-4/PCI system (Physical Acoustics Ltd., USA). Two multi-resonance AE sensors (type WD) and two preamplifiers with 40 dB gain and compatible filter 10 kHz-2 MHz were used to capture the AE signals, which can provide the information in a relative wide frequency range. The frequency response curve of the sensor is shown in Fig. 5 according to ASTM E976 (Ref 29). To eliminate the environmental noise, a threshold of 35 dB was maintained throughout the experiment, which was about 7 dB higher than the background noise level. According to Kaiser effect, this was verified by a dummy specimen repeatedly loading and unloading far below the macro-yield several times. Except during the first cycle of loading, no emission was generated during the subsequent loading, and this ensured that the AE signals were not recorded from the mechanical and external noise.

## 3. Results

### 3.1 Tensile Mechanical Properties

Figure 6 presents the curves of the nominal stress versus the nominal strain. The specimens started necking at a nominal strain of 0.098-0.12. With grain size increased, the elongation, the 0.2% yield stress, and the ultimate tensile stress all decreased; additionally, the macro-yield changed from discontinuous yielding to gradual yielding. This phenomenon has also been observed by Ghaderi (Ref 13). Considering the similar texture state of the three conditions (Fig. 2), there are two possible reasons for the observed variation of the macro-yield with grain size. First is the initial dislocation of the specimens before heat treatment. The  $D = 26 \mu\text{m}$  material was obtained after hot-rolling and stress relief annealing at 673-773 K; this specimen contained many dislocation tangles and had a high mobile dislocation density. However, after heat treatment at higher temperatures and for longer times, as done for  $D = 45 \mu\text{m}$  and  $D = 93 \mu\text{m}$  specimens, the number of dislocation tangles and the mobile dislocation density were both reduced. The second reason is the presence of deformation twinning. At smaller grain sizes, and therefore more grains per unit volume, there is greater probability of finding grains with the proper crystallographic orientation to produce strain in the direction of the applied stress. On the other hand, more twins are needed to accommodate the imposed strain in larger grains; this explanation has been confirmed both theoretically and experimentally (Ref 12, 13). The orientation of the parent grain is changed by deformation twinning, and it is beneficial for continuous slip deformations.

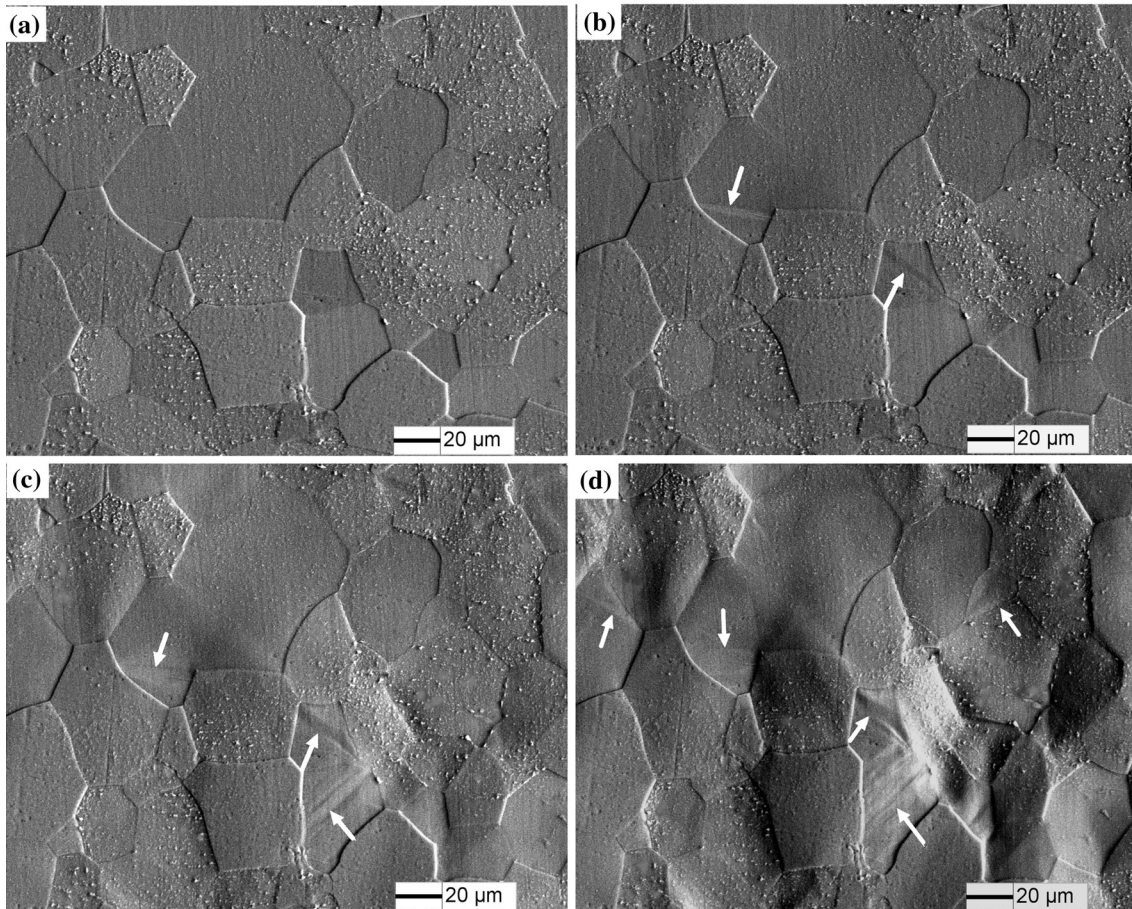
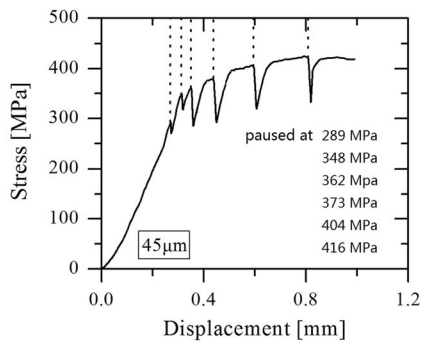


**Fig. 10** Sequential SEM micrographs for the  $D = 45 \mu\text{m}$  specimen at (a) 362, (b) 373, (c) 404, and (d) 416 MPa

The yield and flow stress of metals vary with grain size according to the Hall-Petch equation:

$$\sigma = \sigma_0 + kD^{-1/2}, \quad (\text{Eq } 10)$$

where  $\sigma_0$  and  $k$  are material parameters and  $D$  is the average grain size.

According to Eq 10, the true stress as a function of the inverse square root of grain size is plotted in Fig. 7 for various plastic strains. The method of least squares is used for linear fitting, and the correlation coefficients are shown for each line. It has been reported that the Hall-Petch slope  $k$  for titanium depends on the amount of interstitial alloying content and varies between 6 and 18 MPa mm<sup>1/2</sup> (Ref 10, 11). The  $k$  value in the present study is 15.38 MPa mm<sup>1/2</sup>, whereas  $\sigma_0$  is 236.9 MPa at 0.2% plastic strain. However, at strains of 2 and

4%, the true stress to the inverse square root of the grain size does not show a perfect linear relationship. This indicates that different deformation mechanisms occurred during this stage.

According to the curve of nominal stress versus nominal strain, the whole tensile process can be generally divided into four stages as follows: (1) the elastic deformation stage, during which the nominal stress increases linearly with increasing nominal strain, (2) the macro-yield stage, from the end of the elastic deformation stage to the development of 0.2% plastic strain, (3) the work-hardening stage, between the onset of 0.2% plastic strain and the ultimate tensile strength, and (4) the necking and fracture stage, from the ultimate tensile strength to the tensile fracture. Necking is commonly associated with strain localization and possible initiation of micro-cracking, while fracture is related to micro-cracking extension. Considering the

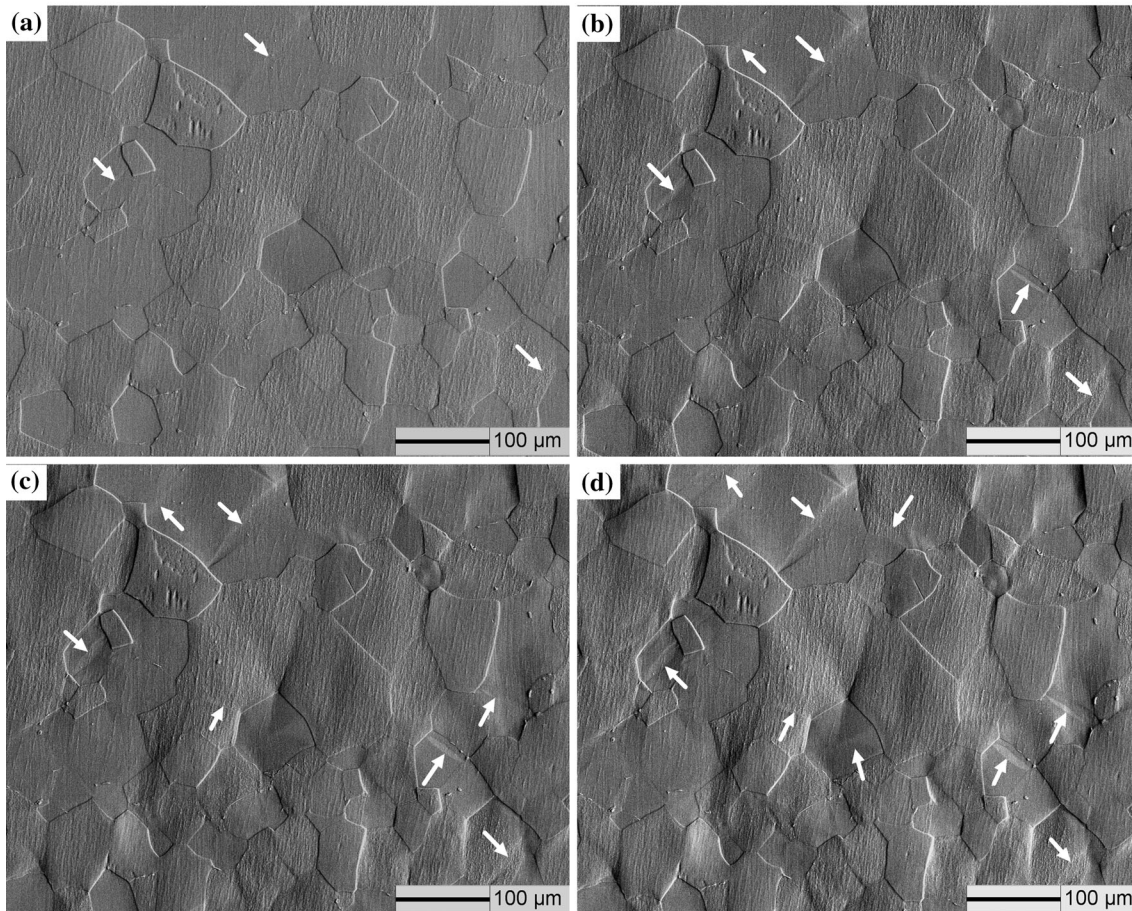
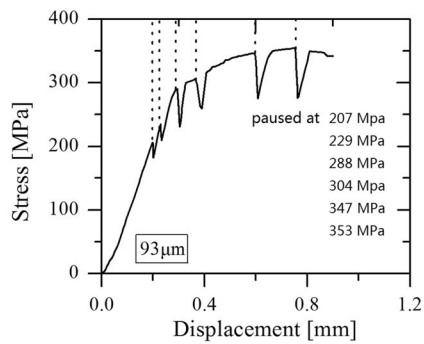


**Fig. 11** Sequential SEM micrographs for the  $D = 93 \mu\text{m}$  specimen at (a) 288, (b) 304, (c) 347, and (d) 353 MPa

present work focused on tensile deformation, the features of the crack and fracture are excluded in the discussion. Thus, the following analysis is restricted to stages 1 through 3, from the onset of tension to the nominal strain of about 0.10.

### 3.2 Micro-structural Characterization

**3.2.1 Optical Observation.** Deformation twinning with lenticular shape was observed in all three grain sizes after tension failure. Based on 1800-2000 grains, the twinning volume fraction ( $T_V$ ) was analyzed statistically as a function of nominal strain for different grain sizes (Fig. 8). It is shown that  $T_V$  increased with the nominal strain; at constant strain levels,  $T_V$  increased significantly with grain size. For the  $D = 26 \mu\text{m}$  specimen, twinning seldom occurred. For the  $D = 45 \mu\text{m}$

specimen,  $T_V$  became saturated before necking. Finally, for the  $D = 93 \mu\text{m}$  specimen,  $T_V$  increased markedly during stage 2 and continued to increase significantly during the late stage of deformation. These results indicate that the deformation mechanism varied with the tensile strain. Although plastic deformation was predominantly governed by slip, the contribution of deformation twinning was grown from weak to evident with the increase of grain size.

**3.2.2 SEM Observation.** To obtain a more intuitive and clear understanding of the evolution of twinning, in situ SEM was used with specimens under tension; part results are shown in Fig. 9-11. None of the specimens were taken to failure. The test was paused for imaging at various stress levels as marked. The observed twins are marked by arrows. In the  $D = 26 \mu\text{m}$  specimen, little twinning occurred after necking. In the

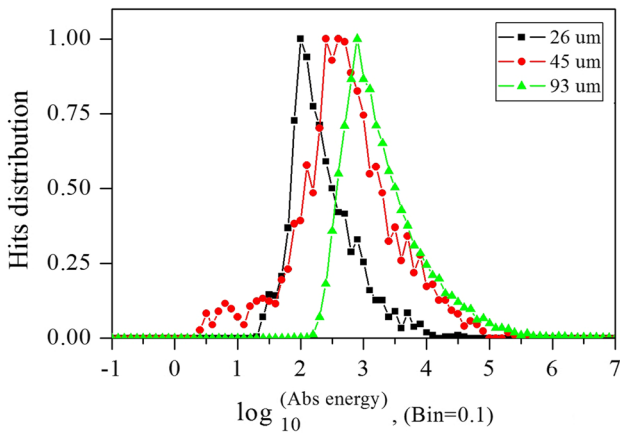


Fig. 12 Normalized distribution of the AE Hits-Abs energy

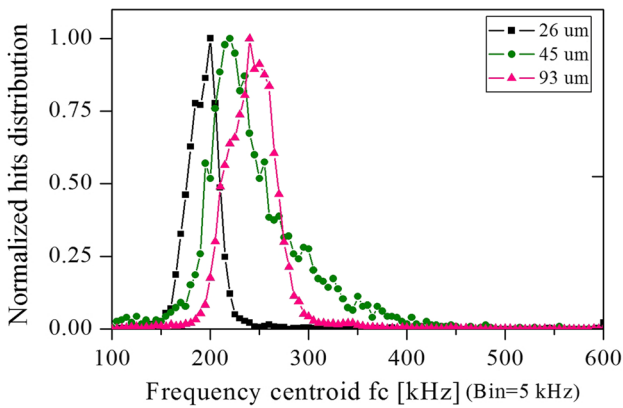


Fig. 13 Frequency centroid distribution for grain sizes of (a) 26, (b) 45, and (c) 93  $\mu\text{m}$

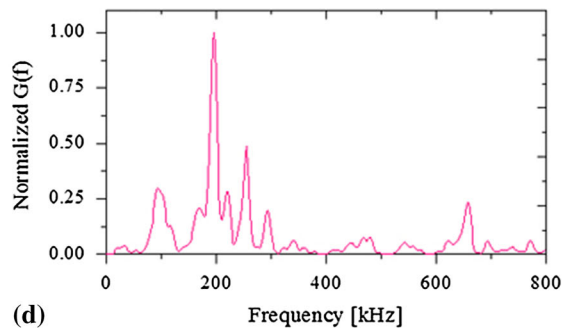
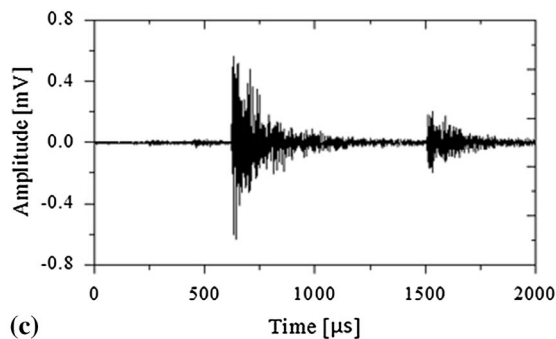
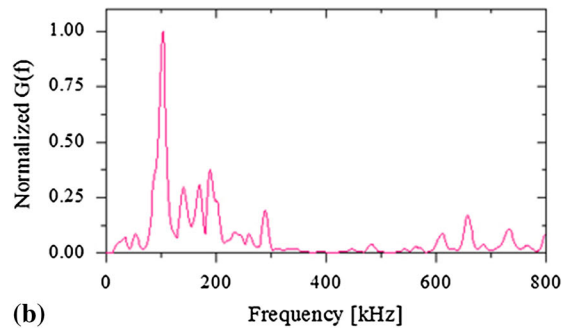
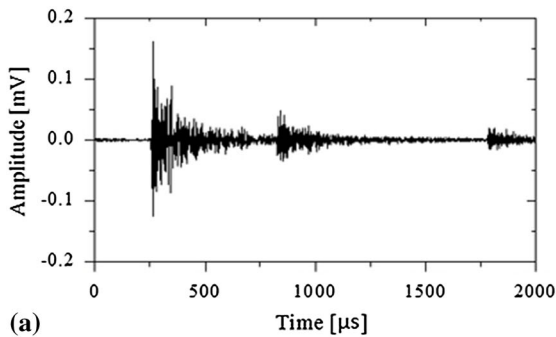


Fig. 14 Typical AE waveform and PSD for cluster 1 (a) and (b), and cluster 2 (c) and (d)

$D = 45 \mu\text{m}$  specimen, some twinning appeared around yield and subsequently increased only subtly. In the  $D = 93 \mu\text{m}$  specimen, more twinning emerged at the onset of plastic deformation and the amount of twinning increased remarkably with strain thereafter. The twinning activities at the yield and the subsequent stage were consistent with the  $T_V$  in Fig. 8, and were captured by the AE monitoring as noted in the discussion.

### 3.3 AE Statistical Results During Tension

In terms of the AE energy, the absolute energy (Abs energy) distributions generated before necking are presented in Fig. 12. Abs energy, whose unit is attojoules (or aJ), is derived from the integral of the squared voltage divided by the reference resistance (10 k $\Omega$ ) over the duration of the AE waveform packet (Ref 30). The distributions are all normalized for comparison. As the grain size increased, the peak of Abs energy distribution shifted to the right. Thus, larger crystal grain generated higher energy of the corresponding AE signals. This result is consistent with the theory and the experimental results for other materials as summarized in section 1.2.

In terms of the AE frequency, the frequency centroid ( $f_c$ ) distributions are illustrated in Fig. 13. It is clearly shown that  $f_c$  shifted to higher values as the grain size grew. As mentioned before, with regard to slip, and as noted by Fleischmann et al. (Ref 23) and Moorthy et al. (Ref 25), the AE frequency will shift to lower values with an increase in the grain size. Here, the fact that higher frequency components increased significantly with the increased grain size indicates that twinning is another important AE source under the test. Additionally, it showed that the predominant AE sources varied from the smaller grain size to the larger grain size. This conjecture can be confirmed by the observations of the microstructures in Fig. 8-11. Thus, it makes sense to evaluate the twinning activity based on the AE activities that come from twinning. Because of the continuous values of  $f_c$ , in order to avoid human intervention, the method



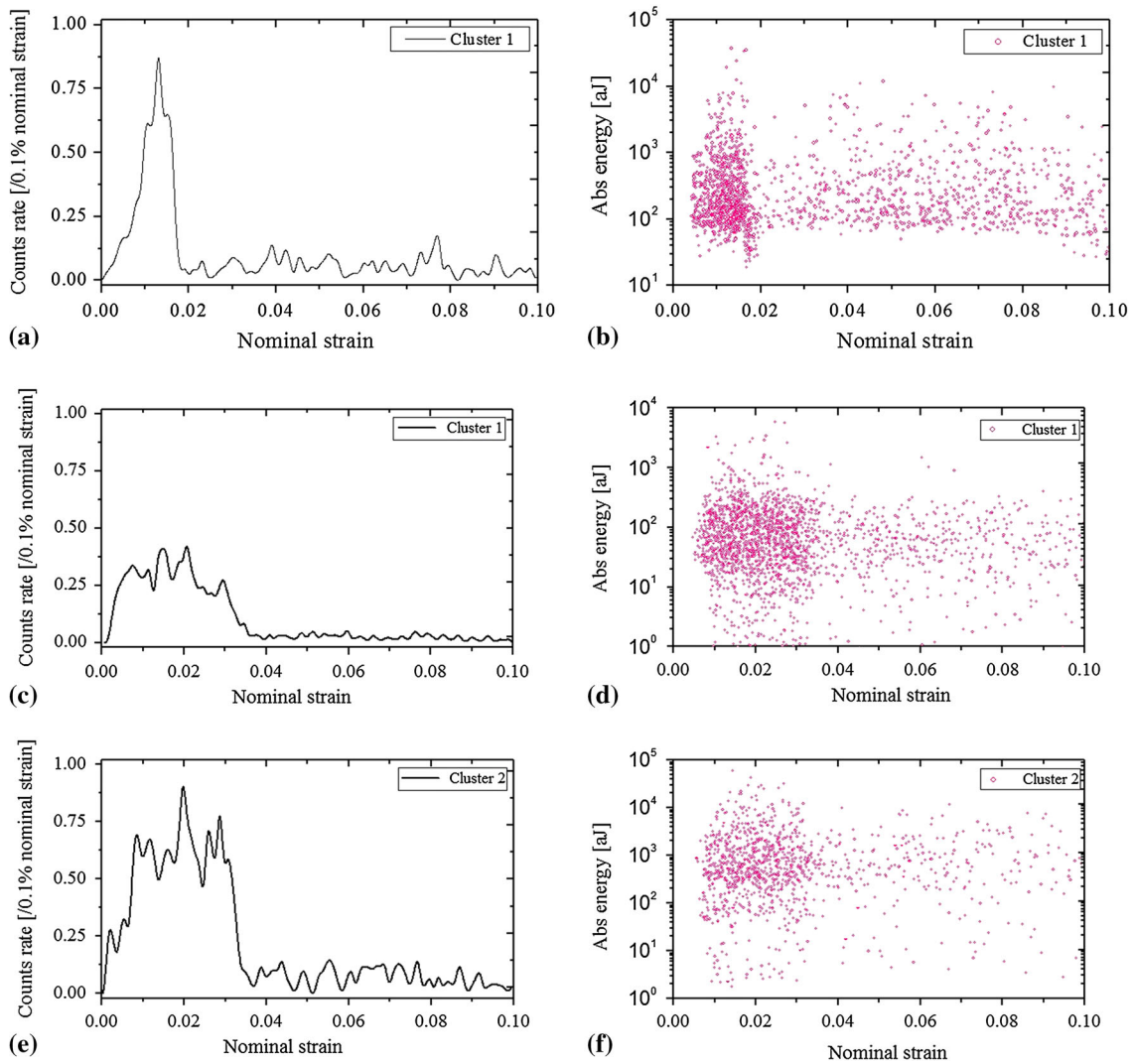


**Fig. 15** AE counts rate and energy vs. strain for two clusters, (a) and (b) for  $D = 26 \mu\text{m}$ , (c) to (f) for  $D = 45 \mu\text{m}$ , and (g) to (j) for  $D = 93 \mu\text{m}$

of pattern recognition was used to separate the AE signals from different physical sources. The details of recognition are discussed in the following.

## 4. Discussion

### 4.1 AE Signal Classification Method

Correct interpretation of the AE data requires properly distinguishing between the AE events stemming from the different sources. In this work, the AE signals from twinning exhibited higher energy and higher frequency components than those of slip. Therefore, the vector of wavelet packet energy coefficient,  $\tilde{X}$ , which reflects the energy of the waveform in different frequency ranges, was set as identifying feature for AE source pattern recognition.  $\tilde{X}$  was calculated by the wavelet packet decomposition (WPD) method (Ref 31), and the Daubechies wavelet was set as the wavelet basis with a

decomposition level of  $n = 5$ . To normalize  $\tilde{X}$ , the coefficient of signal energy in the decomposition level  $m$  was defined as  $X_m = E_m/E$ , where  $E_m$  is the energy of decomposed signal in the  $m$  level, and  $E$  is the total energy of signal. A  $k$ -means clustering method (Ref 32) was applied for AE classification, and  $\tilde{X}$  was used as the input vector. The initial starting points were decided according to Arai and Barakbah (Ref 33). The correlation distance  $d_{CR}$  between two vectors,  $\tilde{X}_i$  and  $\tilde{X}_j$ , was defined as

$$d_{CR} = 1 - \frac{\sum_{m=1}^N (\tilde{X}_{im} - \langle \tilde{X}_{im} \rangle) (\tilde{X}_{jm} - \langle \tilde{X}_{jm} \rangle)}{\sqrt{\sum_{m=1}^N (\tilde{X}_{im} - \langle \tilde{X}_{im} \rangle)^2 \sum_{m=1}^N (\tilde{X}_{jm} - \langle \tilde{X}_{jm} \rangle)^2}} \quad (\text{Eq 11})$$

According to Eq 11, the  $k$ -means algorithm calculated the mean distance  $\bar{d}_{CR}$  between all the AE waveforms and its standard deviation  $\sigma_{d}$ . An intra-cluster distance  $d_{in}$  was

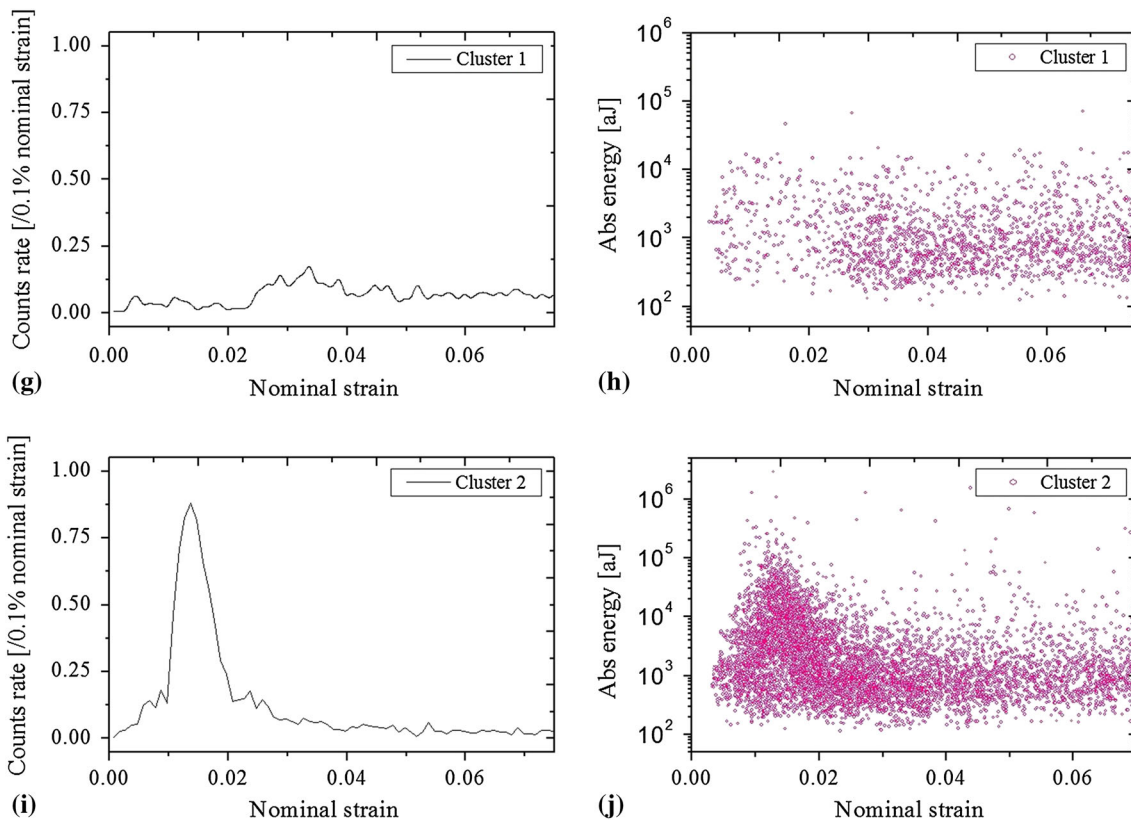


Fig. 15 continued

introduced as  $d_{in} = \overline{d_{CR}} + \mathbf{B}\sigma_{dd}$ , where  $\mathbf{B}$  was a constant between 0 and 5. Thus, the AE waveform was either assigned to the nearest existing cluster or to another new one. Finally, based on the above, all AE signals were assigned to two clusters.

#### 4.2 AE Classification Result

For the two clusters, the typical AE waveforms and their corresponding power spectral density (PSD)  $G(f)$  (Ref 34) are illustrated in Fig. 14. Cluster 1, with its lower frequency, is naturally related to the dominance of dislocation motion, while cluster 2, with its higher frequency and higher energy, is associated with a preponderance of mechanical twinning.

Figure 15 presents the recognition results for different grain sizes between stages 1 and 3. Two generally used AE parameters, the counts rate and the Abs energy of the AE signals, were introduced to describe the activity and intensity of AE behavior. It can be seen that tremendous AE signals were detected mainly around yield, and that after yield, the AE gradually decreased. This trend is similar to previous studies (Ref 15, 16). Considering that slip and twinning having no apparent transition point from the beginning of deformation until fracture, the data of the two AE clusters overlap on the strain scale. For the  $D = 26 \mu\text{m}$  specimen, the AE data classified as cluster 2 were only 0.8% of the data points; these data were sparse and scattered. These results confirm that slip was the predominant mechanism before necking. For simplicity, the cluster 2 result was not shown in Fig. 15. For the  $D = 45 \mu\text{m}$  specimen, clusters 1 and 2 coexisted and occupied

66% and 34% of the data points, respectively. Although the quantity of data points in cluster 2 was smaller than the number in cluster 1, the magnitude of the AE energy for cluster 2 was an order higher than that of the cluster 1. Thus, the increase in count rates during stage 2 can be attributed primarily to twinning. For the  $D = 93 \mu\text{m}$  specimen, the data ratios for clusters 1 and 2 were 22 and 77%, respectively. The predominant mechanism of AE source in the early deformation stages was twinning. After yield, the number of data points in cluster 1 increased markedly (Fig. 15g). This finding implies that slip played more of a role after yield. The characteristics of AE for the three grain sizes are all consistent with the microscopic observations described in section 3.2.

In Fig. 15, the AE counts rate curves exhibited two notable features that also appeared in other hcp metal under tension, such as in magnesium (Ref 27, 35). (i) the AE was detected long before the macro-yield. This is a consequence of the micro-plasticity caused by local slip and/or twinning (Ref 35). (ii) the AE appeared consecutively throughout the entire tensile test, as a result of twinning activity; In carbon steel, the AE reached its maximum just at the macro-yield stage, and only a few AE signals appeared intermittently during the work-hardening stage (Ref 36). Compared to the AE counts rate curves of the three grain sizes, it can be seen that for the  $D = 45 \mu\text{m}$  specimen, the AE curves showed wider peaks with more maximums than the other two specimens. This phenomenon repeated in our repetitive specimens for all grain sizes. It can be ascribed to the grain size probability of the three conditions as shown in Fig. 1. For the  $D = 26 \mu\text{m}$  and  $D = 93 \mu\text{m}$  specimens, the probabilities were both in

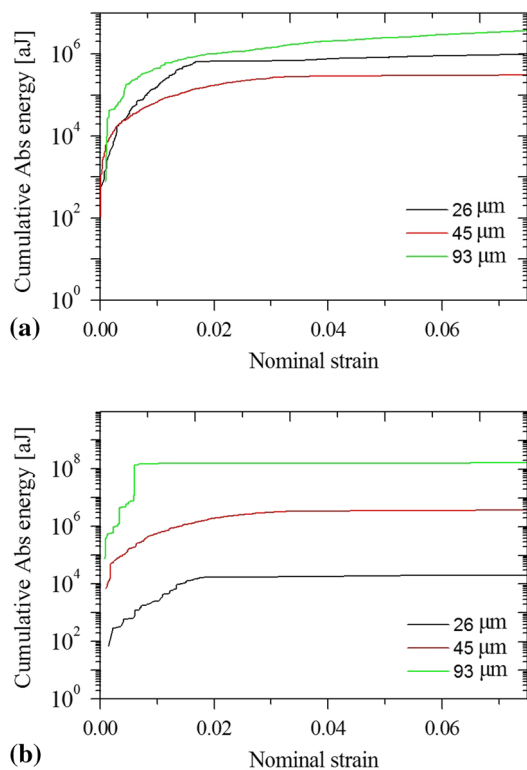


**Fig. 16** Cumulative AE energy for (a) cluster 1 and (b) cluster 2

accordance with a normal distribution, while for the  $D = 45 \mu\text{m}$  specimen, it showed a bimodal distribution. The crystal grains with two main dimensions started their plastic deformation ‘out of step.’ This led to the macro-yield lasting longer time and wider peaks in the AE curves.

Based on the cluster results, the effect of grain size on each deformation mechanism can be discussed respectively. The analysis of strain in terms of the AE cumulative Abs energy ( $C_{ae}$ ) is illustrated in Fig. 16. For Cluster 1, at the beginning of yield, the  $C_{ae}$  increased with the increasing grain size. However, after yield, the  $C_{ae}$  of the  $D = 26 \mu\text{m}$  specimen became higher than that of the  $D = 45 \mu\text{m}$  specimen but lower than that of the  $D = 93 \mu\text{m}$  specimen. The growth in grain size produced a complex of interacting effects on the AE from slip. The result is consistent with the summary by Heiple and Carpenter (Ref 24).

‘For pure materials, the glide distance of dislocation avalanches near the onset of plastic flow is proportional to the grain size, and it tends to increase AE with increasing grain size. Meanwhile, the most likely source of dislocations and dislocation avalanches is grain boundaries. Increasing grain size reduces the grain boundary area, and hence, the number of possible avalanche sources, which tends to reduce AE with increasing grain size.’

Therefore, depending on the grain size, the AE activity caused by slip is not monotonic, and the interaction between slip and twinning needs further research.

For Cluster 2, the  $C_{ae}$  increased with the increasing grain size. This is consistent with the analysis in section 1.2. Moreover, this result is similar to the findings in magnesium, which is another type of hcp metal that can easily produce twinning. As observed in the Mg alloys AZ31 and ZK60

(Ref 14, 28), the highest AE activities were accompanied by the largest grains, which was attributed to the larger size and larger number of mechanical twinning in the larger grains.

## 5. Conclusions

- (1) The CP-Ti specimen with larger crystal grains provided a wider space for slip and twinning, and presented a higher overall AE intensity and activity. The Abs energy and counts rates of the AE signals increased with the increase in crystal grain size.
- (2) The use of the multi-resonant AE sensor with a relative wide frequency response indicated that slip and twinning exhibited different frequency spectrum characteristics. The former showed lower frequency components and a smaller energy than the latter.
- (3) The activities of slip and twinning with applied tension can be compared based on AE signal pattern recognition. For small grains, the predominant deformation mechanism was dislocation slip. For the medium grains, mechanical twinning increased with strain around yield and became saturated before necking, and it contributed to the plastic deformation limitedly. In large grains, many twins appeared in the early stage of deformation, and their number drastically increased thereafter. However, during the later stages of the tensile test, the contribution of slip increased as well.
- (4) As the grain size increased, the AE Abs energy from twinning increased prominently, whereas the AE energy from slip exhibited a non-monotonic change. This result demonstrates that the interaction of slip and twinning varied with the increasing grain size. However, the understanding and quantitative evaluation for this finding need further research.

## Acknowledgment

This study was financially supported by the Chinese 12th five-year project 2011BAK06B03.

## References

1. N. Bozzolo, N. Dewobroto, H.R. Wenk, and F. Wagner, Microstructure and Microtexture of Highly Cold-Rolled Commercially Pure Titanium, *J. Mater. Sci.*, 2007, **42**(7), p 2405–2416
2. N.E. Paton and W.A. Backofen, Plastic Deformation of Titanium at Elevated Temperatures, *Metall. Trans. A*, 1970, **1**(10), p 2839–2847
3. G.T. Gray, III, Influence of Strain Rate and Temperature on the Structure Property Behavior of High-Purity Titanium, *J. Phys. IV Fr.*, 1997, **7**(c3), p 423–428
4. H. Li, D.E. Mason, Y. Yang, T.R. Bieler, M.A. Crimp, and C.J. Boehlert, Comparison of the Deformation Behaviour of Commercially Pure Titanium and Ti-5Al-2.5Sn (wt%) at 296 and 728 K, *Philos. Mag.*, 2013, **93**(21), p 2875–2895
5. M.A. Friesel and S.H. Carpenter, An Inverted Strain Rate Dependence of the Acoustic Emission Generated During the Deformation of High Purity  $\alpha$ -Ti, *Mater. Sci. Eng. A*, 1984, **68**(1), p 107–111
6. W. Tirry, S. Bouvier, N. Benmhenni, W. Hammami, A.M. Habraken, F. Coghe, D. Schryvers, and L. Rabet, Twinning in Pure Ti Subjected to Monotonic Simple Shear Deformation, *Mater. Charact.*, 2012, **72**, p 24–36

7. Y.B. Chun, S.H. Yu, S.L. Semiatin, and S.K. Hwang, Effect of Deformation Twinning on Microstructure and Texture Evolution During Cold Rolling of CP-Titanium, *Mater. Sci. Eng. A*, 2005, **398**(1–2), p 209–219
8. M.E. Nixona, O. Cazacu, and R.A. Lebensohn, Anisotropic Response of High-Purity  $\alpha$ -Titanium: Experimental Characterization and Constitutive Modeling, *Int. J. Plast.*, 2010, **26**, p 516–532
9. M.C. Brandes, M. Baughman, M.J. Mills, and J.C. Williams, The Effect of Oxygen and Stress State on the Yield Behavior of Commercially Pure Titanium, *Mater. Sci. Eng. A*, 2012, **551**, p 13–18
10. H. Conrad, Effect of Interstitial Solutes on the Strength and Ductility of Titanium, *Prog. Mater. Sci.*, 1981, **26**(2–4), p 123–403
11. R.J. Lederich, S.M.L. Sastry, J.E. O’Neal, and B.B. Rath, The Effect of Grain Size on Yield Stress and Work Hardening of Polycrystalline Titanium at 295 and 575 K, *Mater. Sci. Eng.*, 1978, **33**(2), p 183–188
12. M.A. Meyers, O. Vöhringer, and V.A. Lubarda, The Onset of Twinning in Metals: A Constitutive Description, *Acta Mater.*, 2001, **49**(19), p 4025–4039
13. A. Ghaderi and M.R. Barnett, Sensitivity of Deformation Twinning to Grain Size in Titanium and Magnesium, *Acta Mater.*, 2011, **59**(20), p 7824–7839
14. J. Bohlen, P. Dobron, E. Meza Garcia, F. Chmelik, P. Lukáč, D. Letzig, and K.U. Kainer, The Effect of Grain Size on the Deformation Behaviour of Magnesium Alloys Investigated by the Acoustic Emission Technique, *Adv. Eng. Mater.*, 2006, **8**(5), p 422–427
15. H. Tanaka and R. Horiuchi, Acoustic Emission Due to Deformation Twinning in Titanium and Ti-6Al-4V Alloy, *Scripta Metall.*, 1975, **9**(7), p 777–780
16. M. Friesel and S.H. Carpenter, Determination of the Sources of Acoustic Emission Generated During the Deformation of Titanium, *Metall. Trans. A*, 1984, **15**(10), p 1849–1853
17. J. Kumar, S. Punnose, C.K. Mukhopadhyay, T. Jayakumar, and V. Kumar, Acoustic Emission During Tensile Deformation of Smooth and Notched Specimens of Near Alpha Titanium Alloy, *Res. Nondestruct. Eval.*, 2012, **23**(1), p 17–31
18. G. Murasawa, T. Morimoto, and S. Yoneyama, Nucleation and Growth Behavior of Twin Region around Yield Point of Polycrystalline Pure Ti, *Exp. Mech.*, 2012, **52**(5), p 503–512
19. J.B. Chung, “Analysis of Acoustic Emission During Metal Plastic Deformation and Application to Metal Cutting”, Ph.D. thesis, University of Michigan, 1991
20. N. Kiesewetter and P. Schiller, Acoustic-Emission from Moving Dislocations in Aluminum, *Phys. Stat. Sol. A*, 1976, **38**(2), p 569–576
21. C. Scruby, H. Wadley, and J.E. Sinclair, The Origin of Acoustic-Emission During Deformation of Aluminum and an Aluminum-Magnesium Alloy, *Philos. Mag. A*, 1981, **44**(2), p 249–274
22. J. Friedel, *Dislocations*, 1st ed., Pergamon Press, Oxford, 1964
23. P. Fleischmann, F. Lakestani, and J.C. Baboux, Spectral and Energy Analysis of a Moving Ultrasonic Source—Application to the Acoustic Emission of Aluminum Under Plastic Deformation, *Mater. Sci. Eng.*, 1977, **29**(3), p 205–212
24. C.R. Heiple and S.H. Carpenter, Acoustic Emission Produced by Deformation of Metals and Alloys—A Review: Part I, *J. Acoust. Emiss.*, 1987, **6**, p 177–204
25. V. Moorthy, T. Jayakumar, and B. Raj, Acoustic Emission Technique for Detecting Micro- and Macro- yielding in Solution-Annealed AISI, Type 316 Austenitic Stainless Steel, *Int. J. Press. Vessels. Pip.*, 1995, **64**(2), p 161–168
26. B. Woodward and R.W. Harris, The Use of Signal Analysis to Identify Sources of Acoustic Emission, *Acustica*, 1977, **37**, p 190–197
27. Y.P. Li and M. Enoki, Evaluation of the Twinning Behavior of Polycrystalline Magnesium at Room Temperature by Acoustic Emission, *Mater. Trans.*, 2007, **48**(6), p 1215–1220
28. A. Vinogradov, D. Orlov, A. Danyuk, and Y. Estrin, Effect of Grain Size on the Mechanisms of Plastic Deformation in Wrought Mg-Zn-Zr Alloy Revealed by Acoustic Emission Measurements, *Acta Mater.*, 2013, **21**(6), p 2044–2056
29. ASTM Standard E976, Standard Guide for Determining the Reproducibility of Acoustic Emission Sensor Response, ASTM, 2010
30. Physical Acoustics Ltd., Disp with AEwin User’s Manual, 2nd ed., 2003, p 26–28
31. X.H. Wang, C.M. Zhu, H.L. Mao, and Z.F. Huang, Wavelet Packet Analysis for the Propagation of Acoustic Emission Signals Across Turbine Runners, *NDT&E Int.*, 2009, **42**(1), p 42–46
32. M.G.R. Sause, A. Gribov, A.R. Unwin, and S. Horn, Pattern Recognition Approach to Identify Natural Clusters of Acoustic Emission Signals, *Pattern Recognit. Lett.*, 2012, **33**(1), p 17–23
33. K. Arai and A.R. Barakbah, Hierarchical K-Means: An Algorithm for Centroids Initialization for K-Means, *Rep. Fac. Sci. Eng. Saga Univ.*, 2007, **36**(1), p 25–31
34. P.D. Welch, The Use of Fast Fourier Transform for the Estimation of Power Spectra: A Method Based on Time Averaging Over Short, Modified Periodograms, *IEEE Trans. Audio Electroacoust.*, 1967, **15**, p 70–73
35. J. Čapek, K. Máthis, B. Clausen, J. Stráská, P. Beran, and P. Lukáš, Study of the Loading Mode Dependence of the Twinning in Random Textured Cast Magnesium by Acoustic Emission and Neutron Diffraction Methods, *Mater. Sci. Eng. A*, 2014, **602**, p 25–32
36. Z.Y. Han, H.Y. Luo, and H.W. Wang, Effects of Strain Rate and Notch on Acoustic Emission During the Tensile Deformation of a Discontinuous Yielding Material, *Mater. Sci. Eng. A*, 2011, **528**, p 4372–4380